Earth **Surface**
Dynamics
Discussions

Towards a global database of rainfall-induced landslide inventories: first insights from past and new events

Odin Marc[1], André Stumpf[1], Jean-Philippe Malet[1], Marielle Gosset[2], Taro Uchida[3], and Shou-Hao Chiang[4]

[1]École et Observatoire des Sciences de la Terre − Institut de Physique du Globe de Strasbourg, Centre National de la Recherche Scientifique UMR 7516, University of Strasbourg, 67084 Strasbourg Cedex, France
[2]Géoscience Environnement Toulouse,Toulouse,France
[3]National Institute for Land and Infrastructure Management, Research Center for Disaster Risk Management, Tsukuba, Japan
[4]Center for Space and Remote Sensing Research, National Central University, Taoyuan City 32001, Taiwan

Correspondence: Odin Marc (odin.marc@unistra.fr)

Abstract. Rainfall-induced landslides are a common and significant source of damage and fatality worldwide. Still, we have very little understanding of the quantity and properties of landsliding that can be expected for a given storm and a given landscape, mostly because we have very few datasets of rainfall-induced landslides. Here we present six new comprehensive landslide inventories associated to well identified rainfall events. Combining these datasets, with two previously published datasets, we study their statistical properties and their relations to topographic slope distribution and storm properties. Landslide metrics (such as total landsliding, peak landslide density or landslide distribution area) vary across 2 to 3 order of magnitudes but strongly correlate with the storm total rainfall, varying over almost 2 orders of magnitude for these events. Correlation increases when we apply a normalization on the landslide runout distances. The non-linear scaling with total rainfall should be further constrained with additional cases and incorporation of landscape properties such as regolith depth, typical strength or permeability estimates. We also observe that, for storm with longer duration, landslides do not occur preferentially on the steepest slopes of the landscape, contrarily to observations from earthquake-induced landslides, suggesting preferential failures of larger drainage area patches with intermediate slopes. The database could be used for further comparison with spatially resolved rainfall estimates and with empirical or mechanistic landslide event modeling.

Copyright statement. TEXT

1 Introduction

Landslides associated with heavy rainfalls cause significant economic losses and may injure several thousand people a year worldwide (Petley, 2012). In addition, the frequency of landsliding increases with that of extreme rainfall events (Kirschbaum et al., 2012), itself expected to increase with global change (Gariano and Guzzetti, 2016). Landslides are also recognized as a major geomorphic agent contributing to erosion and sediment yield in mountainous terrain (Hovius et al., 1997; Blodgett and

Isacks, 2007). Yet, constraining quantitatively relationships between landslides and rainfall metrics remains out of reach.

We have some theoretical understanding of how rainfall, through water infiltration in the ground, can increase pore water pressures and trigger failures (Van Asch et al., 1999; Iverson, 2000). Therefore a variety of mechanistic models have been developed, usually by coupling a shallow hydrological model to a slope failure criterium (e.g., Montgomery and Dietrich, 1994;

5 Baum et al., 2010; Arnone et al., 2011; Lehmann and Or, 2012). However, such deterministic approaches require not only appropriate physical laws, but also an accurate and fine-scale quantification of many input parameters (topography, cohesion, permeability, rainfall pattern)(Uchida et al., 2011). At this day, such level of detailed information is unavailable in most places and render deterministic approaches inapplicable.

Data-driven studies have mostly focused on using precise information on individual landslide location and timing to decipher

10 thresholds, typically based on preceding rainfall intensity and duration, at which landslide would initiate (Caine, 1980; Guzzetti et al., 2008, and references therein). Although useful for hazard and early-warning purposes (e.g., Keefer et al., 1987), such approaches completely ignore the number, size and other properties of landslides that can be triggered by a rainfall event, while these properties are useful, if not required for most natural hazard or geophysical applications. In order to understand the importance of rainfall on erosion rates or to anticipate landslide hazard associated with emerging cyclones and heavy rainstorms,

15 it is highly desirable to quantitatively relate the properties of a landslide event $\mathbf{L}$ (total area, volume, size distribution) to the combination of site susceptibility, $\mathbf{s}$, and rainfall forcing, $\mathbf{f}$, properties, or equivalently to develop scaling relations of the form of:

$$\mathbf{L} = g(\mathbf{s}(slope,\ soil\ thickness,\ strength,\ permeability,...), \mathbf{f}(total\ rainfall,\ intensity,\ antecedent\ rainfall,...))\quad (1)$$

Although being simplified versions of mechanistic models, such scaling laws can be useful to describe average properties

20 of the phenomena, here a population of landslides associated with a constrained trigger. The value of statistical or semi-deterministic approaches is that they are able to predict accurately global properties, while circumventing the difficulties of predicting specific local properties of individual landslides. Indeed, such scaling laws would allow to make prediction in data scarce region and possibly at various scales (large slope scale, catchment scale, region scale, etc). This approach has driven important progress for both the understanding and hazard management of earthquake-induced landslides, thanks to the intro-

25 duction of purely empirical, physically inspired or mixed functional relations in the form of Eq. 1 (e.g., Jibson et al., 2000; Meunier et al., 2007, 2013; Nowicki et al., 2014; Marc et al., 2016, 2017). These progresses have been possible thanks to, first detailed investigation of individual case studies with comprehensive landslide inventories (e.g., Jibson et al., 1994; Liao and Lee, 2000; Yagi et al., 2009) and next through their combined analysis as aggregated databases (Marc et al., 2016, 2017; Tanyaş et al., 2017).

30 In contrast, very few studies on rainfall induced landslides are based on comprehensive inventories. Some studies are based on individual landslide information. For example, Saito et al. (2014) studied 4744 landslides in Japan, that occurred between 2001 and 2011, to better understand which rainfall property controls landslide size. This dataset, aggregating small subset of the landslides triggered by rainfall events, misses the vast majority of landslides (for example, in Japan, Typhoon Talas alone caused a similar amount of landslides in a few days). It is therefore insufficient for more advanced statistical analyses. At global

scale, Kirschbaum et al. (2009), presented a catalog containing information on 1130 landslide events worldwide, occurring in 2003, 2007 and 2008. With this catalog they underlined the correlation between extreme rainfall and landsliding (Kirschbaum et al., 2012). However, such catalogs, mainly based on reports from various kinds, gather very fragmentary knowledge, and contain little quantitative information on landsliding. Thus, we consider that neither landslide scale or global scale studies are

5   sufficient to constrain effectively Eq 1, and that storm scale detailed information are needed.

Although relatively rare, some case studies at the catchment scale exist (and are briefly reviewed in the next section) but they rarely constrain the whole region affected by the storm, and thus . However, in theory, satellite imagery allows comprehensive mapping of landslides larger than the resolution limit, across all catchments affected by a large storm. In practice, obtaining useful images strictly constraining the landsliding caused by a single storm is not always possible, mainly because of cloud

10   coverage, and detailed mapping across vast areas represent a significant work effort. As a result, landslide inventories triggered by rainfall during a whole season or a few years are used for testing mechanistic models (e.g., Baum et al., 2010; Arnone et al., 2011).

The purpose for this paper is to present a compilation of new and past comprehensive rainfall-induced landslide (RIL) inventories, each representing adequately the landslide population associated with an identified storm. They constitute the core of an

15   expandable database, essential for further research. We first briefly review existing comprehensive and partially complete inventory associated with specific storms. Then we present six new inventories and analyze their statistical properties in terms of size, geometry and relation to topographic slopes. We further analyze and discuss the properties relative to rainfall observations in those cases and conclude on the various insights that can be derived from such inventory compilation.

2   Data and methods

20   ### 2.1   Review of pre-existing dataset

An in-depth literature review revealed that very few comprehensive, digital, RIL inventories have been published, such as the Colorado 1999 and Micronesia 2002 events detailed below. If we look for partial inventories, in which landslides have been mapped comprehensively in limited zones affected by a storm, a few more datasets exists.

For example, hurricane Mitch hit central America at the end of 1998 and triggered thousands of landslides across several coun-

25   tries. The rainfall were record breaking in many places, with rain gauges recording up to 900, 1100 and 1500 mm in Honduras, Guatemala and Nicaragua (Bucknam et al., 2001; Cannon et al., 2001; Crone et al., 2001; Harp et al., 2002). In the following weeks, the USGS performed an number of air-surveys, identified the most affected areas in these three countries as well as in El Salvador (where the rainfall amount was less), and mapped a large number of the failures based on aerial photographs. The resolution of the optical imagery allowed to distinguish failures down to a relatively small size ($< 100 m^2$), but the mapping

30   amalgamated multiple failures into single polygons, and combined very long debris flow paths and/or channel deposits to the source areas. Last, the mapping was only performed in a number of isolated areas, that were "the most affected", and it is unclear how much landsliding was present in the unmapped zones. Because of these limitations, we did not investigate this case in details here but note that these inventories may be corrected and used by later studies. Similarly in a number of studies,

inventory of all the landslides caused by a given storm in a specific catchment or geographic zone can be found, in Liguria 2000 (Guzzetti et al., 2004), Umbria 2004 (Cardinali et al., 2006), Sicily 2009 (Ardizzone et al., 2012), Peru 2010 (Clark et al., 2016), Thailand 2011 (Ono et al., 2014) and Myanmar 2015 (Mondini, 2017) and in Taiwan for ten typhoons between 2001 and 2009 (Chen et al., 2013). The issues for these partially complete datasets is whether or not the statistical properties of the

5 subset are representative of the entire dataset associated with the storm and its specific properties. There is no doubt that a number of these datasets could be completed based on available satellite imagery and later complement the database presented here.

In this study we analyzed two datasets published previously by the USGS. First, an afternoon rain on the 28th of July 1999 that triggered numerous landslides and debris flows in the Colorado front range (Godt and Coe, 2007). Based on aerial

10 photographs interpretation and field inspection, landslides were mapped as polygons containing source areas, debris flow travel and deposition zones. 57 out of 328 polygons were associated to multiple sources (2 to > 15). Often the largest of these polygons represent 61% of the total landslide area. As the surface of the source areas were often of similar width, we decided to conserve multi-headed polygons and to consider each sources contributed equally. Thus, we use the whole landslide area, A_l, perimeter, P_l, and number of source, N_s, for each multi-headed polygon to derive an equivalent area and perimeter associated

15 with each source: $A_s = A_l/N - s$ and $P_s = P_l/N_s$. This first order approach underestimates the perimeter of each components by one width (the segment that would be added for each necessary split), however this underestimation decreases with the length/width ratio of the polygons, and is already below 10% for $L/W > 4$. In any case, this assumption does not affect the total area affected, but it changes the landslide frequency-area and frequency-width distributions, and all terms derived from them.

20 The second dataset contains landslides caused by a summer typhoon in July 2002, mapped exhaustively with aerial photos on the islands of Micronesia (Harp et al., 2004). We digitized the original maps based on strong contrast between red polygons and the rest of the maps. A few artifacts due to this image processing were removed and a few amalgams were split. Again, scarps and deposits are not differentiated.

2.2 New comprehensive inventories of rainfall-induced landslides

25 We present the mapping methodology and imagery (Table Suppl. 1) used to produce six additional inventories. In 2008 around the Brazilian town of Blumenau, several days of intense rainfall at the end of a very wet fall triggered widespread landsliding and flooding, with some partial inventories published in the Brazilian literature (e.g., Pozzobon, 2013; Camargo, 2015) but no analyses in the international literature. The detection and manual mapping of landslides as georeferenced polygons was primarily done with a pair of Landsat 5 cloud free images (02/01/2009 and 03/02/2008). The coarse resolution (30m) of

30 the images allowed only to locate vegetation disturbances and accurate landslide delineation was only possible for the largest events. Therefore we used extensively high-resolution imagery available in Google Earth acquired in May-June 2009, and when not available in 2010-2012, where scars were still visible. We mapped only the ones corresponding to vegetation radiometric index (e.g. NDVI) reduction for the pair of Landsat 5 images. Thus the landslide mapping could be confirmed for ∼90% of the mapped polygons, and man-made digging or deforestation occurring on steep slopes could be avoided. This approach avoid

amalgamating groups of neighboring landslides and to map very small landslides ($\sim$1 pixel in Landsat 5 images). However, some detailed field mapping in the surrounding of Blumenau reports up to twice more landslides than we observed (Pozzobon, 2013) indicating that we still miss a number of small events. Nevertheless, these landslides must be quite small (not visible in $\sim 1m$ resolution imagery) and likely do not affect any of our statistics (area, volume, slope) apart the total number of

5 landslides.

The same approach was used to map the intense landsliding caused by a few days of intense rainfall between the 10th and the 12th of January 2011 (Netto et al., 2013), in the mountains northeast of Rio de Janeiro. Near Teresopolis, we used first a pan-sharpened (10m) EO-ALI and a Landsat 7 images from February 2011 for co-registration and ortho-rectification. $> 95\%$ of the slides were cross-checked in Google Earth (Fig 1) and where clouds or no images where available we mapped landslides

10 directly from Google Earth, even if poor ortho-rectification may create geometric distortions. Closer to Nova Friburgo, we used a pair of very high resolution Geoeye-1 image presented in Stumpf et al. (2014), and extended the methods presented in their study to classify the whole image. Then, we screened manually the image to remove false positive (agricultural field, inundated areas, channel deposits) and split the amalgamated landslides, very frequent given the important clusters of landslides in many part of the image. This correction seems sufficient given that landslide size distribution for the three subparts of the inventory

15 are consistent (Fig. Suppl. 1). Polygons from the automatic classification display a slightly larger equivalent length/width ratio, maybe because some amalgamated polygons have been missed or simply because the classification allows hollow polygons, biasing upward the length/width estimate based on a perimeter/area ratio (see below).

In the first days of September 2011 (1st-4th), typhoon Talas triggered very heavy rainfall on the Kii Peninsula, in Japan, resulting in several thousands of landslides. For disaster emergency response, the National Institute for Land and Infrastructure

20 Management of Japan mapped landslides across most of the affected areas based mainly on post-typhoon aerial photographs and occasionally on Google Earth imagery (Uchida et al., 2012). Screening antecedent imagery (2010-2011) from Google Earth and Landsat 5 we identified and removed a few hundreds pre-Talas polygons, mostly within 5km of 136,25°E/34,29°N and 135,9°E/34,20°. With Google Earth we added almost 200 polygons in areas were aerial photographs were not taken, and split many large or multi-headed polygons that were amalgamated. Some polygons had distorted geometry or exaggerated

25 width, most likely due to poor ortho-rectification of the aerial imagery and/or time-constrains for the mapping. We could not systematically check all polygons, but we checked and corrected all polygons larger than $30,000m^2$ (3% of the catalog but representing 45% of the total area). We consider that the remaining distortions for some of the smaller polygons have minor impacts on the statistics discussed in the next sections.

In Taiwan, we collected landslide datasets associated with the 2008 Kalmaegi (16-18th Jul.) and 2009 Morakot (6-10th Aug.)

30 typhoons, partially described by Chen et al. (2013). For 2008, we compared multispectral composite images and NDVI changes between Landsat 5 images taken on the 06/21, 07/07 and 07/23. The image from 07/07 is covered by clouds and light fog in many parts but allows identifying that most places affected by landslides in the last images were still vegetated at this time. Thus all new landslides, delineated manually, are attributed to the rainfall from typhoon Kalmaegi. For 2009, landslides were delineated manually by comparing surface reflectivity and morphology on pre- and post-event FORMOSAT-2 satellite images

35 (2 m panchromatic and 8 m multi-spectral) (Chang et al., 2014). To cover most of the island, we mosaicked multiple mostly
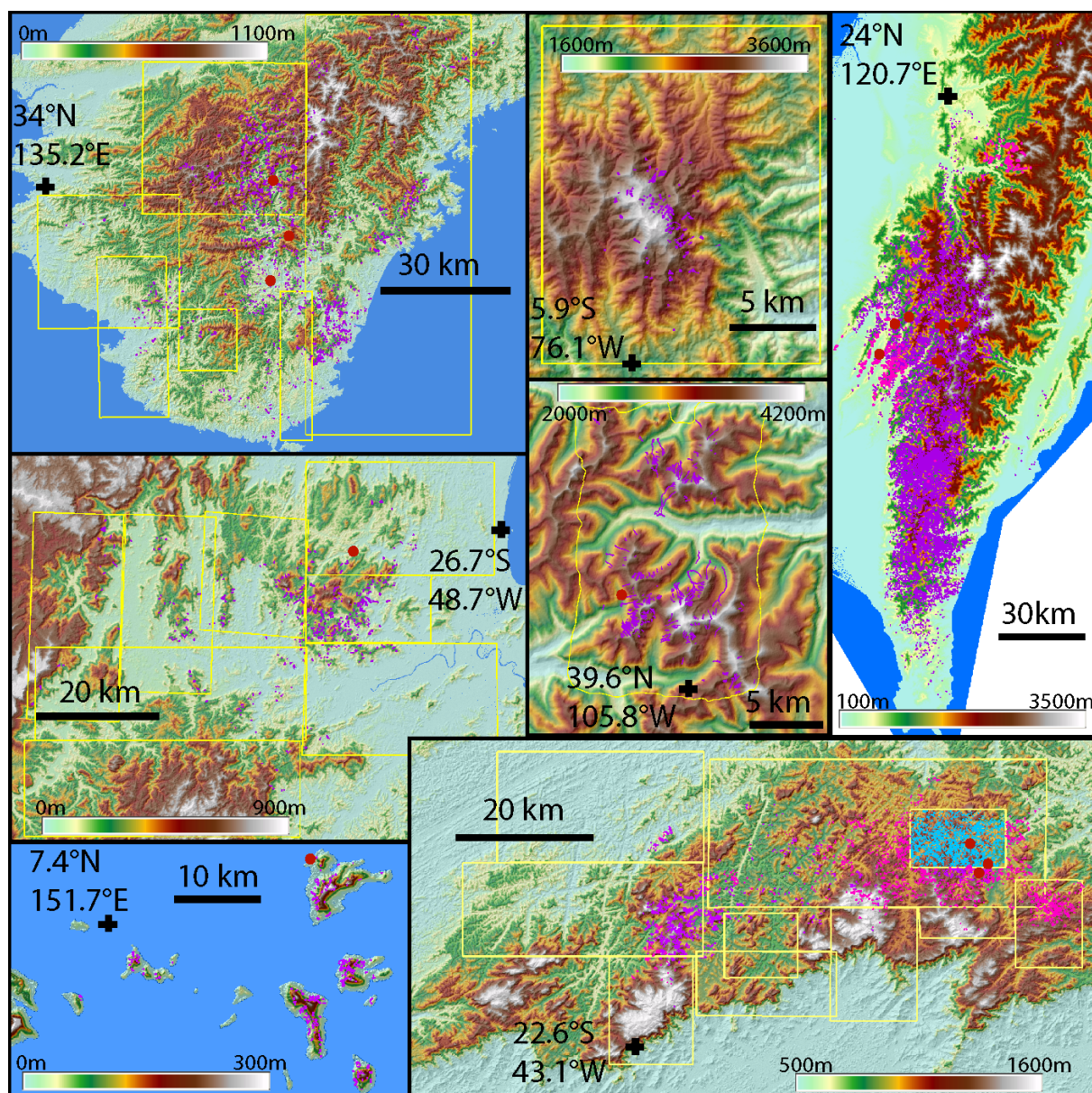
Earth **Surface**
Dynamics
Discussions

Figure 1. Landslides inventory superimposed on digital surface model for the events in Japan 2011 (A), Brazil 2008 (B), Micronesia 2002 (C), Colombia 2015 (D), Colorado 2002 (E), Brazil 2011 (F) and Taiwan 2008 and 2009 (G). Landslides are in purple, rain gauges used in this study are in red dots (and red crosses for Taiwan 2009), and the yellow frames show the availability of high resolution imagery (Google Earth) used to check or perform the mapping. In G, the pink dots are landslides from 2008, while purple dots are from 2009. In F, purple, pink and cyan are landslides mapped from EO-ALI, Google Earth and automatic classification of Geoeye image, respectively.

cloud-free pre-event (01/14, 05/08, 05/09, 05/10, 06/06) and post-event (08/17, 08/19, 08/21, 08/28, 08/30, 09/06) images. For sub-parts of the inventory, especially to the East of the main divide, landslides were first mapped automatically and then edited manually. For both approaches, the scar, runout and deposit areas are not differentiated. We did not consider debris flow transport within the fluvial system and ignored gentle slopes ($< 10°$) from mapping to avoid confusion with human activity.

5 In a few areas with clouds in the post-event mosaic, we used Landsat imagery to be sure to map at least the largest landslides. Special attention was given to the separation of individual landslides by systematically checking and splitting polygons above $0.1 km^2$ (2% of the catalog but representing 30% and 60% of the total area and volume). However, it is clear that a number of smaller slides are missed or merged with large ones, and therefore although total landsliding and landslide locations on slope may be well represented, the size distribution of this catalog must be biased to some extent.

10 Between 15 and 17th of May 2015, heavy rainfall in the mountains above the village of Salgar, Colombia, triggered catastrophic landslides and debris flow (>80 deaths). Landslide mapping was carried out by comparing a Sentinel 2 image from 2016 to a 2014 Landsat 8 image. These images were selected for their absence of clouds, good conditions of light and similarity. Other intermediate images in between those show very little activity before or after May, supporting the idea that all mapped landslides can be attributed to this single rainfall event.

15 ## 2.3 Rainfall data

Rainfall data quality and amount are very variable for the different events, from 0 or 1 single gauge (For Micronesia or Colombia), to dense gauge network and potentially weather radar coverage in Japan, Taiwan and Brazil. Therefore we selected a simple index that could be obtained for each case in order to discuss potential rainfall controls on the landslide properties. For each case we calculated an estimate of total rainfall, R_t, duration, D, and a peak rainfall intensity over 3 hours, $I3$ (Table 1).

20 Note that these variables do not represent an average value within the whole footprint of the storm but rather maximal forcing, usually where landsliding was the most intense (Fig 1), derived mostly from one or a few rain-gauges. A more detailed analysis of the spatio-temporal pattern of the rainfall and of its relations to the spatial pattern of landsliding is highly desirable, but challenging with the available dataset. Indeed, some cases with little in-situ information may be best studied by a combination of meso-scale rainfall modeling possibly assisted by satellite information, while other would require integration and processing of

25 extensive rain-gauges and radar measurements. For this study, we limit our scope to the analysis of specific landslide behavior and to the proposition of a series of research hypotheses that could be later investigated with very detailed inventories and adequate rainfall analyses.

The estimates from Taiwan and Japan are based on hourly gauge measurements from the Japan Meteorological Agency and Taiwan Institute for Flood and Typhoon research. In each case we took the three closest gauges within 5 to 15km from the

30 areas with the highest landslide densities (Fig Suppl. 2) and computed their average record properties (Fig 2). Minimum and maximum single gage measurements give a coarse measure of the uncertainty. A single gauge is available in Micronesia and we used the hourly rainfall from 1st to 3rd of July 2002 reported in Harp et al. (2004). For Colorado, we used the hourly rainfall from the rain gauge at Grizzly peak, closest of intense landsliding and reported by Godt and Coe (2007). For the event in Brazil 2008 we considered the total daily rainfall from Luis Alves station (Fig 1), where more than 130mm per day were accumulated

Table 1. Rainfall data summary, containing the total rainfall, duration and maximum 3-hours intensity for each storms. For TW8, TW9 and J11, we indicate the range for the three indexes that could be estimated from three gauges near the zone of maximal landsliding. We cannot perform this analysis for MI2 and C99, and can only assess a range of R_t for B08 and B11. For C15, we indicate by a star that we could only access satellite based rainfall estimates (GSMaP version 7 ungauged products, see Fig Suppl. 3). Reference are as follow, 1: (Godt and Coe, 2007), 2: (Harp et al., 2004), 3:(Camargo, 2015) , 4:(Netto et al., 2013) .

Event	C99	MI2	B08	TW8	TW9	B11	J11	C15
R_t, mm	45	500	695[680-800?]	670[600-740]	2500[2100-2800]	280[200-320]	1300[1000-1500]	65[10-75]*
D, hours	4	20	100	24	100	36	65	10*
$I3$, $mm.hr^{-1}$	13	65	30	92[78-116]	85[83-87]	55	58[38-88]	8*
Ref.	1	2	3	Us	Us	4	Us	GSMaP

on the 21st, 22nd and 23rd of November and 250mm on the 25th, and intensity going up to 50mm/hr (Camargo, 2015). These days were also preceded by abnormally wet period, with November 2008 accumulating $\sim 1000mm$, 7 times the long term average for this month. In 2011 in Brazil, hourly rain data at Sitio Sao Paulista reports 200 mm in 8 hours before gauge failure, while there and at nearby sites, the cumulative rainfall was $\sim 280mm$ from the 10th to the morning of the 12th January (Netto

5 et al., 2013). For these cases, raingages give a trustworthy estimate of the local rainfall, but are not constraining the large scale rainfall pattern. Last, in Colombia, we could not find data from any nearby rain-gauge and we thus use rainfall estimates from the GSMaP global satellite products (Kubota et al., 2006; Ushio et al., 2009) (Fig Suppl. 3). Here, the minimum, mean and maximum rainfall are obtained by considering the triggering storm as the raining period at the time of debris flow occurrence, or the one from the previous day or merging both events, respectively (Fig Suppl. 3).

10 Defining storm duration accurately requires defining thresholds on rainfall intensity other given periods, to delimit the storm start and end. Given the variable quality of our data we limit ourself to a first order estimate of the continuous period when rainfall was sustained. We consider these durations accurate within 10-20% for the events with overall hourly data. For the less constrained cases B08, B11 and C15 duration is more uncertain. In any case, for these 8 storms, we note a strong correlation between D and R_t and $I3$ and R_t (for power-law scalings, $R^2 = 0.8$ and $R^2 = 0.7$, respectively). Thus, given that spatial and

15 temporal length scales are often linked in meteorology, the long events causing larger rainfall may also have larger footprints.

2.4   Landslide area, width and volume

Landslide planview area and perimeter are directly obtained from each polygon. However, these values represent the total area disturbed, that is the scar, deposit and runout areas, because a systematic delineation of the scar was not possible from most of

20 the imagery. This means that landslide size statistics is resulting from processes affecting both landslide triggering and runout. Landslide volume, estimated based on area, may also be overestimated for long runout slides. Therefore we propose here a simple way to normalize for landslide runout and obtain an estimate of the scar area.

Following Marc and Hovius (2015), we computed an equivalent ellipse aspect ratio, K, using the area and perimeter of each
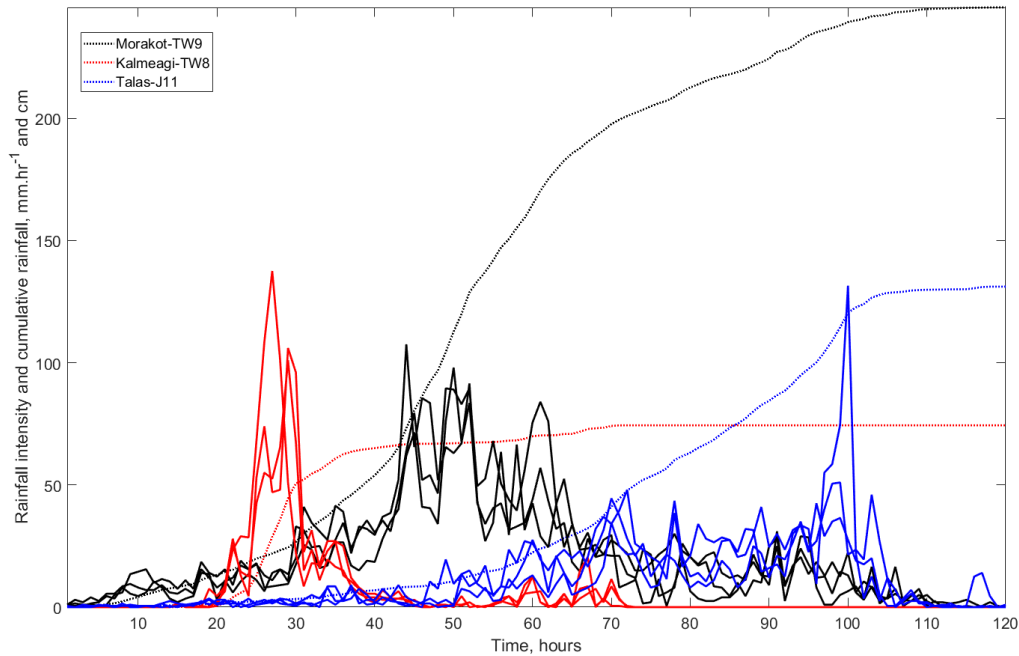
Figure 2. Rainfall history for typhoons Kalmaegi (TW8), Morakot (TW9), Talas (J11). For each event, hourly intensity is shown with solid curves for three gauges nearby the area with most intense landsliding (see Fig 1 for locations). Dashed lines represent the mean cumulative rainfall from the three gauges.

polygons. For polygons with simple geometries, K is close to the actual length/width ratio, but this is a measure that also increases with polygon roughness or branching, and therefore with amalgamation (Marc and Hovius, 2015). An ellipse area can be approximated by $\pi LW/4$ with L and W being the polygons full length and width, respectively. This allows to estimate $W \simeq \sqrt{4A/\pi K}$. Again, this value is close to the actual mean width of polygons that do not have artifacts. Thus for correctly

5   mapped polygons we can use width to derive a proxy of landslide scar area, $A_s \sim W^2$. Although this equivalent scar area may not exactly correspond to the real landslide scar, it effectively removes the contribution of the landslide runout to the landslide size and allows to compare different size distributions while reducing the impact of variable runout distances.

We also assessed how using A_s affects estimates of landslide volumes and erosion, by computing landslide volume with the total landslide area and with A_s only. In both cases, we used $V = \alpha A^\gamma$, with α and γ and their 1σ globally derived by Larsen

10 et al. (2010). Given that soil and bedrock slides have different shape and that soil slides are rarely larger than $10^5 m^2$ ($10^4 m^2$ for soil scars) (Larsen et al., 2010), we used the "all landslide" parameters ($\gamma = 1.332 \pm 0.005$; $log_{10}(\alpha) = -0.836 \pm 0.015$) when $A < 10^5$, and the "bedrock" parameters ($\gamma = 1.35 \pm 0.01$; $log_{10}(\alpha) = -0.73 \pm 0.06$) for larger landslides. Similarly we used the soil scars ($\gamma = 1.262 \pm 0.009$; $log_{10}(\alpha) = -0.649 \pm 0.021$) and bedrock scars ($\gamma = 1.41 \pm 0.02$; $log_{10}(\alpha) = -0.63 \pm 0.06$) for $A_s < 10^4 \ m^2$ and $A_s >= 10^4 \ m^2$, respectively (Larsen et al., 2010). Marc et al. (2016) proposed a rudimentary version of

such a runout correction, where they effectively reduced landslide area by a factor 2 for mixed landslides and 3 for bedrock landslides, noting that volumes derived in this way were closer to field estimates for large landslides than without correction. Uncertainties in this approach include the 1σ variability of the coefficient and exponent of the landslide area-volume relations given above, and an assumed standard deviation of 20% of the mapped area. These uncertainties were propagated into the

5   volume estimates using a Gaussian distribution. The standard deviation on the total landslide volumes for the whole catalogs or for local subsets, were calculated assuming that the volume of each individual landslide was unrelated to that of any other, thus, ignoring possible co-variance. Although estimated 2σ for single landslides is typically from 60 to 100% of the individual volume, the 2σ for the total volume of the whole catalog is below 10% for the eight datasets. However, for subset with less landslides and with volume dominated by large ones, typical when we compute the total landslide volume density in small area

10   (e.g., 0.05°),2σ uncertainties reaches 40-60%. We note however, that these uncertainties estimates do not consider potential errors in the identification of landslides, either missed because of occasional shadows or clouds or erroneously attributed to the storm. Such uncertainty is hard to quantify but must scale with the area obscured in pre- and post-imagery. In most cases multiple pre- and post-event images mean that obscured areas represent typically less than 10% of the affected area, and such errors may be between few to $\sim 20\%$ of the total area or volume, depending on whether obscured areas contain landslide

15   density higher or lower than the average observed throughout the affected area. Last, resolution may not allow to detect the small landslides and in some cases the landslide number may be significantly underestimates, but not the total area and volume dominated by the larger landslides.

Last, for each inventory, we estimated the landslide distribution area, that is the size of the region within which landslide are distributed. Based on the landslide inventories we could delineate an envelope containing the overall landsliding. As discussed

20   by Marc et al. (2017), such delineation is prone to high uncertainties as it is very dependent on individual isolated landslides. Thus for all cases, we give a range of distribution area, where the upper bound is a convex hull encompassing all the mapped landslides, while the lower bound is an envelope ignoring isolated and remote landslides, if any. Although the spread can be large in absolute value, both approaches yield the same order of magnitude.

3   Results

25   The built inventories contain from ~ 100 to $> 15,000$ landslide polygons, representing total areas and volumes from 0.2 to $200 km^2$ and 0.2 and $700 Mm^3$, respectively. The triggering rainfalls are characterized by a total precipitation of ~ 50 to 2500 mm in period ranging from 4h to 4 days, and caused landslides within areas ranging from ~ 50 to $10,000 km^2$. Although the dominant landslide types are soil and regolith slumps, a number of large deep-seated bedrock landslides are also present in the inventories associated to the Talas and Morakot typhoons (Saito and Matsuyama, 2012; Chen et al., 2013). A more detailed

30   description of the landslide types and materials involved was not possible with the available imagery; thus our analysis does not consider landslide types. In the next sections, we present results obtained from these inventories in terms of landslide size statistics, landslide spatial patterns and relation to slope, before correlating these landslide properties to rainfall parameters.

Earth **Surface**
Dynamics
Discussions

3.1 Landslide properties

3.1.1 Landslide size statistics

Frequency size distribution of landslide inventories typically have power law, heavy-tail, above a certain modal size (Hovius et al., 1997; Malamud et al., 2004). The modes and the decay exponents of these distributions are mainly related to the

5 lithology (mechanical strength) or topographic landscape properties (i.e., susceptibility related) (Stark and Guzzetti, 2009; Frattini and Crosta, 2013; Katz et al., 2014; Milledge et al., 2014). Some authors suggested that this behavior could also be affected by the forcing processes. For example analyzing earthquake induced landslide catalogs, it was found that deeper earthquakes, thus with weaker strong-motions, have a smaller proportion of large landslides (Marc et al., 2016). Based on theoretical arguments, it has been proposed that short high intensity rainfall could cause pulses of high pore water pressures

10 at the soil-bedrock transition, initiating mainly small shallow landslides, while, long duration rainfall with important total precipitation could provoke significant elevation of the water table and trigger large, deep-seated landslides (Van Asch et al., 1999). To our knowledge, only few empirical evidences have supported these assumptions, and we discuss next how our data compare to these ideas.

All landslide size distributions present a roll-over and then a decay that may be fitted by a negative power-law function (Fig

15 3). The modal landslide area varies between $\sim 3000 \ m^2$ for TW8 and $\sim 300 \ m^2$ for B11, while the largest landslides are $\sim 0.1 \ km^2$ for most events and reach ~ 0.4 and $2.8 \ km^2$ for J11 and TW9, respectively. The roll-over position certainly relates partly to the spatial resolution and acquisition parameters of the images (Stark and Hovius, 2001)(e.g., for TW8 and B08 where landslides where mostly mapped on coarse spatial resolution image compared to aerial photographs for C99, J11). However, physical parameters must also control the roll-over position given that, for example, MI2 mapped with 1m resolution

20 aerial imagery has larger modal area than C15 mapped with 10 m Sentinel-2 satellite imagery. The fit of the power-law decay beyond the mode or of the whole distributions with an Inverse-Gamma distribution (IGD) (cf, Malamud et al., 2004) gives decay exponents ρ between 2 and 3, consistent with the typical range found in the literature (Hovius et al., 1997; Malamud et al., 2004; Stark and Guzzetti, 2009; Frattini and Crosta, 2013). However, we note that at least three cases, B11, TW9 and C99, have peculiar distributions, with a break in the distribution occurring at large areas, and followed by a very steep decay.

25 For these cases, the IGD gives a rather poor fit for the largest areas, and the normalized difference in decay exponent between a least-square fit of the tail and the IGD maximum likelihood is larger than the typical $\sim 10\%$ uncertainties on the exponent determination (21, 25 and 66% respectively, against $6 \pm 5\%$ for the five other cases).

When considering landslide estimated scar sizes, that is essentially a correction to reduce landslide polygon aspect ratio below 2, we observe a reduction of the largest landslide size by 2 to 10 fold, but a moderate reduction of the mode size. This

30 is consistent with the fact that landslides with long runout distances are often over represented within the medium to large landslides (Fig Suppl 4). We also note that after the runout distances variability is normalized, the peculiar size distribution of C99 disappears and least-squares fits and IGD give decay exponents identical within a few percent. This is not the case however for B11 and TW9 that still feature a steepening of their distribution decay (and a divergence from IGD fit) beyond $\sim 10^3$ and $\sim 10^4 \ m^2$, respectively. Runout being normalized, this could be an artifact relating to residual amalgamation for TW9, but not
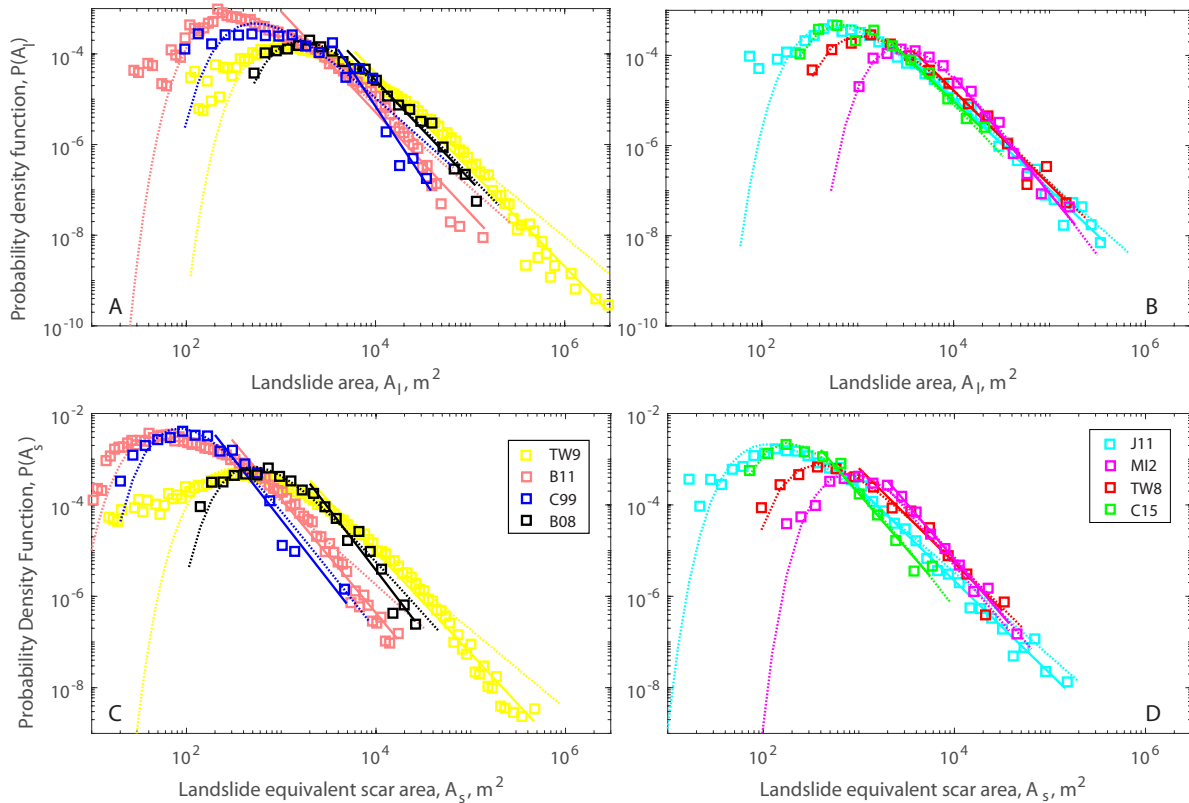
Figure 3. Probability density functions of landslide whole area (A, B) and estimated scar area (C, D). A least square power-law fit of the tail and an IGD maximum-likelihood estimation for the whole distribution are shown by solid and dashed lines respectively.

for B11 where most landslides were mapped manually and amalgamation was avoided. Thus, this peculiar distribution may be the fingerprint of some physical phenomena but no reasonable hypotheses may be assumed so far.

3.1.2 Landslide and slope distribution

For all cases, we computed the frequency of slope angles above 5° based on the global 1 arc-second ($\sim 30m$) SRTM digital
5 surface model. In most cases, hillslopes have a distribution clearly independent from valley floors. However, for B08 and MI2 for example, the amount of plains in the study area do not allow to resolve the hillslope distribution. Therefore, for Micronesia we removed all slopes which are less than 10 m above sea-level, and for Brazil, we extracted the slope cells in the landslide distribution area but with a mask excluding the wide valley bottoms. The slope distributions of landslide affected areas generally lead to a sparsely populated histogram, and therefore, to compare it with the topographic distribution, all histograms were
10 smoothed with a moving average in a window of 3° width.

We obtain topographic modal slopes, S_M, at 15.5° and 18.5° for the gentle landscape of Micronesia and Brazil, while in Japan and Taiwan we reach almost 30° (Fig 4). The slope distributions of landslide affected areas are systematically shifted towards

steeper slopes. In most cases the landslide distribution has a very small shift, but for the C99, B11 and C15 rainstorms the shift is more pronounced with a landslide modal slope $\sim 5°$ larger than S_M. We note that, for the landslide distribution, the proportion of slopes gentler than the topographic mode may be exaggerated due to the inclusion of deposition areas. This is most significant for the C99 case, but also possibly affecting MI2 or B11. For C99 we have also extracted the slope at the

5   initiation point and found this distribution to have a similar mode and decay beyond it than the whole landslide distribution (Fig 4).

To further quantify the differences in slope sampling between these events, we computed the ratio of probability between the slope distribution of the whole topography and of the landslide affected area only, P_L/P_T. This ratio represents the tendency of landslide occurrence to be more or less frequent than the expected occurrence of a slope gradient units in the landscape. We

10 refer to this as and over or undersampling of the topographic slope distribution. To focus on landslide triggering and on the scar areas, we plot this ratio only for $S > S_M$ and against $S - S_M$ to compare the events in different landscape (Fig 5A).

Most events (in Taiwan, Japan, Micronesia) actually maintain an almost equal sampling across all steep slopes. We neglect the important variations present for some cases at slopes 30 to 40° steeper than S_M, as they may be artifact due to the small absolute number of cells in this value range. However, B08, B11, C99 and C15, diverge strongly from equal sampling. The latter

15 three have a remarkably similar pattern, with undersampling at the mode and a rapid increase with steeper slopes until a 3 to 10-fold oversampling between ~ 15 and 30° beyond S_M. This shows that additionally to a steeper landslide mode, landslides are increasingly more frequent on very steep slopes, typically reaching a maximum of oversampling between 40° and 60°. In contrast, in B08 we observe undersampling starting at 10° beyond the mode and reaching a 5-10-fold undersampling beyond 20°.

20

3.2   Correlation between rainfall metrics and landslide properties

3.2.1   Total landsliding

For the eight inventories, we observe a non linear increase of all metrics of total landsliding with the storm total rainfall (Fig 6). The increase is fairly similar for the total area and volume, and best fit by exponential functions. We observe higher correlations

25 with rainfall, when using the total scar area ($R^2 = 0.78$), estimated as W^2, instead of the total area ($R^2 = 0.72$). This is mainly due the very large reductions of area for C99 and B11 where long runout landslides were dominant (Fig 6). Correlation are generally higher with volume and also increase when we derive total volume from scar estimates (from $R^2 = 0.81$ to $R^2 = 0.87$). Note also that with these scar metrics, the relation to rainfall becomes equally or better fit by power-law function rather than an exponential function (Fig 6). This is because when including landslide runout the total landsliding of C99 and C15 is larger

30 and create an apparent asymptote, better fit by an exponential function. Last, we note that total volume values may change depending on which A-V scaling relations is used and with which assumptions, and their absolute values may be inaccurate but this should not affect much the reported scaling form and exponents as potential biases should be relatively uniform.

Total number of landslides also tends to increase with total rain but the scatter is much larger. This is at least partly an artifact,
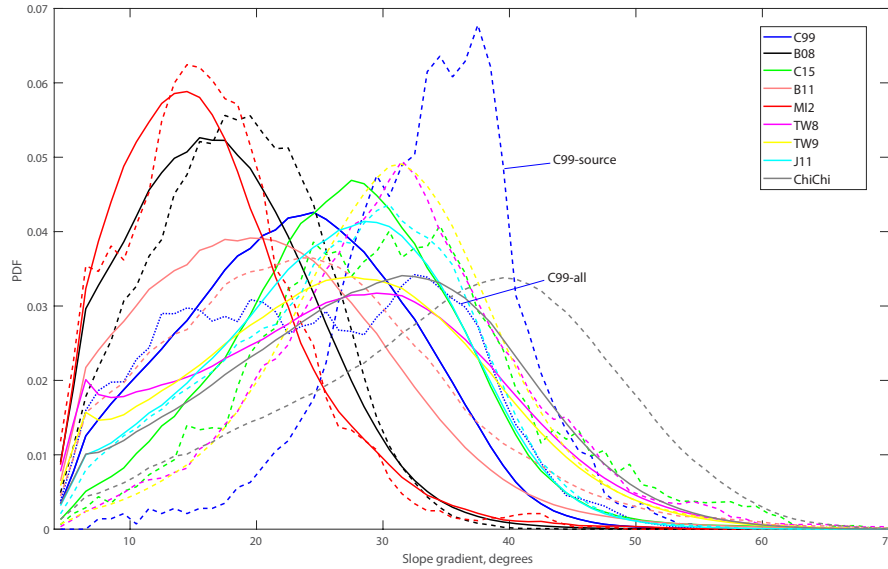
Figure 4. Slope gradient probability distribution for the affected topography (solid) and the landslides affected areas only (dashed), for the eight rainfall events and as a comparison to the Chi-Chi earthquake. For C99 we have a landslide distribution for the landslide including deposit and for source point only.

given that for C99, MI2 and B11, high resolution imagery allows to delineate many more small landslides and to mitigate amalgamation, whereas for B08, TW8 and TW9, the limited spatial resolution, the density of landsliding and our limited ability to split amalgamated landslides lead to an underestimation of the landslide number. Thus, even if landslide number may contain information, quantitative comparisons of the different events are biased and we will not further interpret the total number of

5   landslides in the following.

Last, we note that the landslide distribution areas (i.e., the regions within which landslides are distributed) also correlate strongly with the total rainfall. Only considering the eight inventories strongly suggest a power law form. However, based on the dataset reported for the Hurricane Mitch, the distribution area was at least 100,000 km^2, for maximum total rainfall at about 1500mm (Cannon et al., 2001). Adding it to our fit, we found that power-law or exponential functions of the rainfall explained

10 similar amount of the variance, 72% and 63% respectively.

In the next subsection, we compute landslide densities (in % of area), allowing to study the intra-storm variability of landsliding.

3.2.2   Maximum and mean landslide density

Understanding what controls landslide density is a key objective to better constrain hazards and their consequences. For each

15 storm we compute the mean landslide density (in area and volume) by dividing total landsliding by the landslide distribution area (Fig 7A). This density represents the whole affected area and hides important spatial variability (Fig 1), thus we also com-
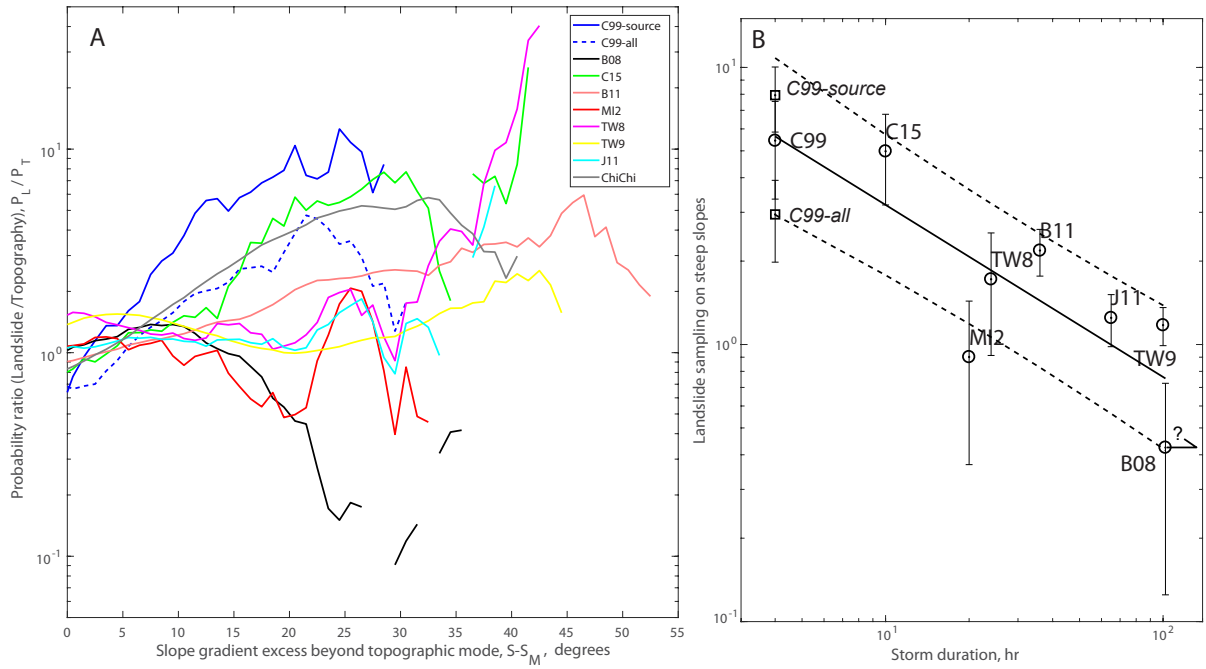
Earth **Surface**
Dynamics
Discussions

Figure 5. (A) Ratio of the two probability distributions against the difference between slope gradient and the modal topography. We display two curves for C99 landslides, the dash-dotted one from the whole landslide area, including deposits, and the other from source point only. (B) Anti-correlation between the steep slope sampling (that is the mean of P_L/P_T for $S - S_M$ in $[15, 30]$) and storm duration. Solid and dashed lines are the best power law fit of the data, averaging C99-all and C99 source into 1 data point ($R^2 = 0.7$). We indicate with an arrow that B08 duration may be underestimated.

pute the maximum landslide density, by computing the total landsliding (again in area and volume) within a moving window of $0.05°$ ($\sim 25 km^2$), assigning landslides to a cell based on their centroid locations, and selecting the maximal value (Fig 7B). Given the better correlation obtained above with a runout normalization, we focus on area and volume densities derived from scar estimates.

5 The mean landslide densities vary between $0.01 - 1\%$ and $100 - 10,000 m^3.km^{-2}$ but with poor correlation with total rainfall ($R^2 = 0.01$ and $R^2 = 0.46$ for area and volume density respectively). Indeed, given that both total landsliding and distribution area increase strongly with total rainfall, their ratio is relatively independent. In contrast, the maximum landslide scar density and volume density range from 0.1 to 5% and 0.002 to 1.5 millions $m^3.km^{-2}$, respectively, and are strongly correlated with a power-law of total rainfall ($R^2 = 0.76$ and $R^2 = 0.95$). We found very similar correlations when computing the local den-

10 sity on a grid of $0.03°$ or $0.1°$, but degraded correlations when using the whole landslide area to compute landslide density ($R^2 = 0.40$ and $R^2 = 0.69$). We also note that, as for the total landsliding, maximum landslide density and volume density are significantly correlated with peak rainfall intensity, $I3$ ($R^2 = 0.58$ and $R^2 = 0.67$, respectively), and duration, D ($R^2 = 0.70$

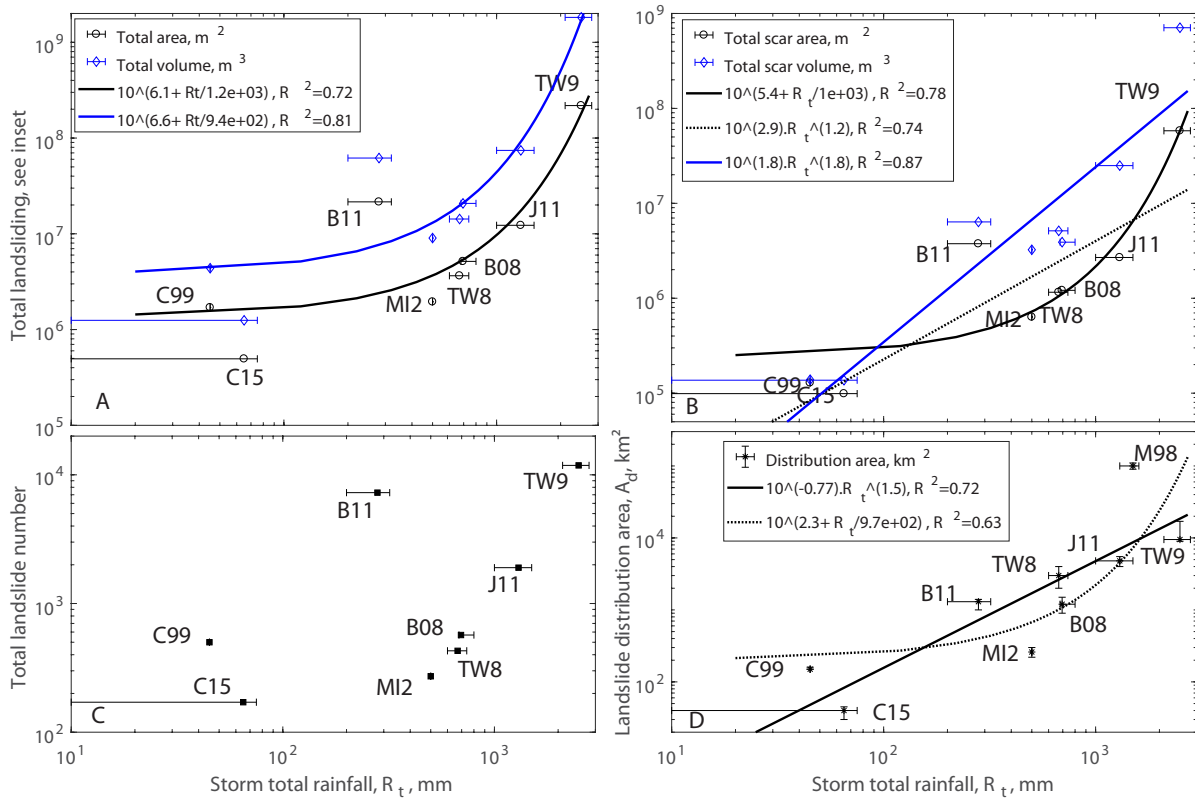Earth **Surface**
Dynamics
Discussions

Figure 6. Total landsliding in area and volume derived from whole landslides (A) or from scar estimates only (B), total landslide number (C) and landslide distribution area (D) against storm total rainfall. M98 is for Mitch 1998. Horizontal error bars show a range of maximum storm rainfall when available (cf, Table 1). In A and B 1σ uncertainty on the total volumes and areas, ignoring potential landslide mis-detection (cf. methods), are smaller than the symbols ($< 10\%$). Vertical error bars are based on the range of affected areas in D, while we could not obtain quantitative uncertainties on the total number (C).

and $R^2 = 0.73$, respectively), although less strongly than with total rainfall.

3.2.3 Landslide size, runout and position on slope

The power-law decay exponents of the distribution of landslide size or equivalent aspect ratio (Fig 3, S**??**) do not correlate
5 significantly with any storm metrics (Intensity, duration or total rainfall) ($|R| < 0.2$). Indeed, long runout landslides are abundant for the smallest storm, C99, as well as for the second largest storm, J11, but are less frequent for the other storms (e.g., MI2,TW8, B08), spanning the whole range of storm indexes.

However, we note that the events where landslides occurred preferentially on steep slopes correspond to very short duration rainfall events (C99 and C15), while the events with the strongest undersampling of steep slopes are the longest storms (B08).
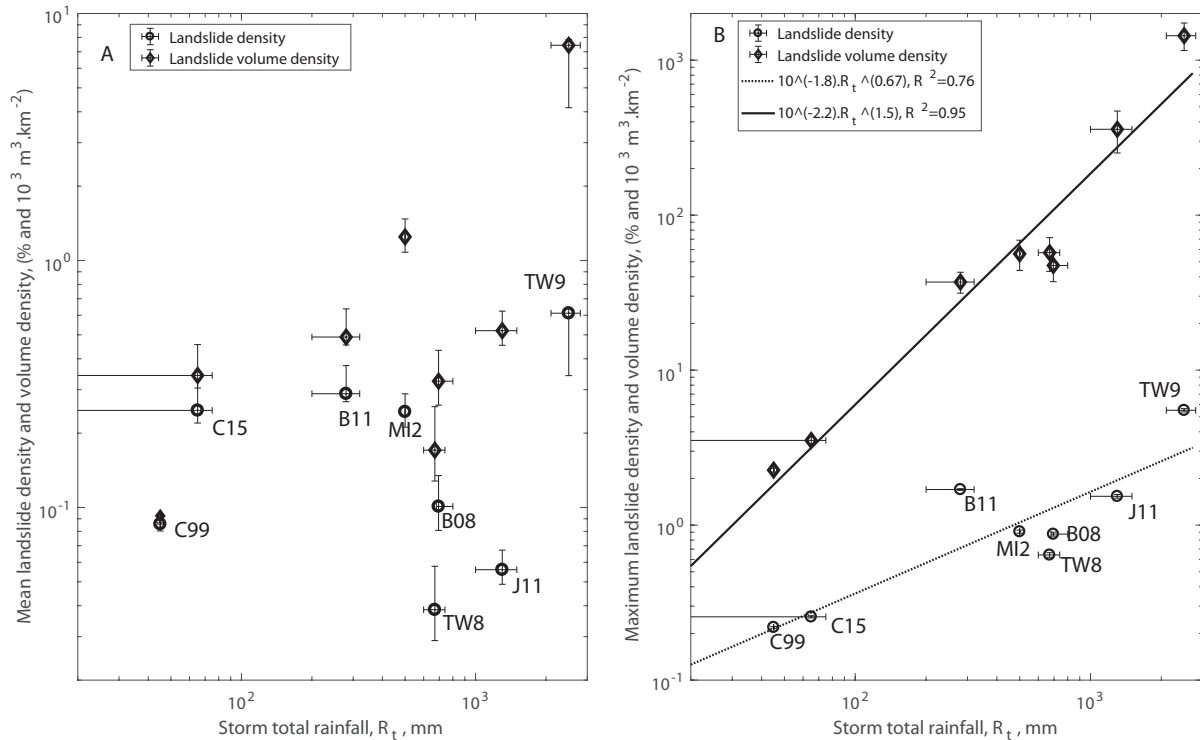
Earth **Surface**
Dynamics
Discussions

Figure 7. Mean landslide density (A) and peak landslide density in a 0.05° sliding window (B), against storm total rainfall. Landslide area and volume are derived from scar estimates, i.e., removing runout contribution. Horizontal error bars shows a range of maximum storm rainfall when available (cf, Table 1). Vertical error bars are based on the range of affected area in A (the most uncertain term), and represents 1σ uncertainty on the total volume and area density in B, ignoring potential landslide mis-detection (cf. methods).

Indeed, if we compute the mean landslide/topography sampling ratio between 10 and 30° above the local topographic mode, we find a correlation of this index with storm duration. A power-law fit is most appropriate and explains $\sim 70\%$ of the variance (Fig 5). This correlation may even be underestimated considering that the Brazil 2008 storm, occurred after several weeks of anomalously elevated rainfall, suggesting a longer duration.

5

4 Discussion

4.1 Scaling between rainfall and landsliding

We found that total landsliding, peak landslide density and the distribution area of landsliding were all best described as increasing as a power-law or exponential function of the total storm rainfall, R_t. Our mechanistic understanding of landsliding

10 predicts that, for a given site, the driving force leading to failure is the reduction of normal load and friction due to the increasing

pore water pressure (Iverson, 2000). This requires progressive saturation of the material above the failure plane, and depends directly on the total amount of water poured on the slopes. The antecedent rainfall is also expected to play a key role, in controlling the saturation level before the triggering storm (e.g., Gabet et al., 2004; Godt et al., 2006). However, if the regolith is already close to the field capacity, significant parts of antecedent rainfall may be drained from the regolith within some hours

5 or days (Wilson and Wieczorek, 1995), and as result, the contribution of past storms may be negligible compared to heavy rainfalls over relatively short time intervals (1-4 days). However, for moderate storms, like C15 or C99, and especially during dry periods when the slope is saturated below field capacity, the role of antecedent rainfall may be more substantial. Thus, we expect that moderate storms happening after prolonged dry or wet periods may deviate downward or upward from the scaling, respectively. We also note that an abundance of larger and deeper landslide strongly influencing the total volume or erosion,

10 may depend on deeper water level rather than regolith saturation and thus may be most sensitive to water accumulation over several days rather than a few hours (Van Asch et al., 1999; Uchida et al., 2013). Therefore, although we obtained a good correlation without considering antecedent rainfall, its role should be assessed in future refined scalings. Last, the scaling reported here is based on events where all landslides occurred within a short time frame (few hours to few days), and would not apply to a monsoon setting where landslides occur more or less continuously during several weeks (Gabet et al., 2004; Dahal

15 and Hasegawa, 2008), driven by continuous, heavy but unexceptional, rainfall.

The strong correlation between R_t and distribution area, suggests that storms able to generate greater amounts of rainfall also tends to deliver a sufficient amount of rain over broader areas. We have no clear physical explanation of why this could be the case, and cannot exclude that it is a coincidence allowed by our small number of events. In any case the broader zone is not likely to receive homogeneous rainfall amount, decoupling mean landslide density from storm maximum strength (Fig 7A).

20 The variability of rainfall within these extended zones is likely a main control on the spatial variability of landslide density, although lithological properties or slope distribution may also matter. Indeed lithological boundaries, or a lack of steep slopes can sometimes explain spatial variability in landsliding, but not all of it (Fig Suppl. 6). In any case, it seems clear that to predict the spatial variability of landsliding, the rainfall spatio-temporal pattern is a prime requirement. The good correlation between storm total rainfall and peak landslide density, is encouraging and suggests that, as most mountainous regions may

25 have sparse instrumental coverage, the use of satellite measurements (Ushio et al., 2009; Huffman et al., 2007) or meso-scale meteorological models (e.g., Lafore et al., 1997) may be required.

A few non-linear scaling between total landsliding and total rainfall have been reported at the catchment scale, but were derived from datasets not easily comparable to the one presented in this study (Reid, 1998; Chen et al., 2013; Marc et al., 2015). The details of this scaling is of importance in order to understand the impact of extreme rainfall events and more generally which

30 type of rainfall event contributes most to sediment transfer over long time scales (Reid and Page, 2003; Chen et al., 2015). We also found non-linear scaling between R_t and total landslide area, but without a strong statistical difference between exponential or power-law. Exponential functions yield a minimum landsliding amount at low rainfall, that is not physical justified. This apparent contradiction may, however, be resolved by considering a rainfall threshold below which landsliding is null. The higher correlation between R_t and total volume, is likely due to the fact that R_t correlates very well with maximum landslide

35 size ($R^2 = 0.8$ with whole landslides, $R^2 = 0.9$ and almost linear correlation with scar estimates, Figure Suppl 5), with large

landslides contributing most of the total volume and erosion. A correlation between R_t and large landsliding may arise because landslide stability is determined by the ratio between pore pressure and the total normal stress on the slip plane, meaning that larger landslides that have usually deeper failure planes (Larsen et al., 2010), may only fail with greater precipitation amount. However, given that we do not observe a clear trend between total rainfall and size distribution, a competing hypothesis may

5   be that this correlation is just a sampling bias as the probability to draw large landslides increases with the total number of landslides. For now, our unreliable estimates of total landslide number do not allow to test this alternative.

The scaling with rainfall may also be obscured by outliers due to processes not controlled by rainfall. For example, the inclusion of the very long runout components in several inventories led to larger scattering for both power-law and exponential models and to favor the latter. Therefore, the proposed runout correction seem essential for future studies. Another issue concerns the

10   normalization of landscape parameters affecting the susceptibility to landsliding, such as hillslope steepness and mechanical strength (Schmidt and Montgomery, 1995; Parise and Jibson, 2000; Marc et al., 2016). The impact of hillslope steepness may be difficult to include as it seems to vary with the type of storms (Fig 5), as discussed below. Nevertheless, the proportion of flat or submerged land within the area of the most intense rainfall must limit the total landsliding, as it was certainly the case for MI2 or B08 (Fig 1). Recent, widespread antecedent landsliding may also reduce subsequent susceptibility to rainfall triggering

15   by removing the weak layer of soil on steep slopes. In the pre-event imagery we did not see specific evidence of such limitation, except maybe for J11, where abundant pre-event fresh landsliding were visible near 136,25°E/34,29°N and 135,9°E/34,20° and very few new landslides occurred. More systematic evaluation of this effect may be important when comparing quantitatively landslide and rainfall pattern. In any case, it is clear that further analysis of this database, possibly extended with additional landslide inventories, should be used by future studies to refine the scaling with rainfall and incorporate the effects of controlling

20   parameters such as available topography, antecedent rainfall or regolith properties (e.g., strength and permeability).

4.2   Relation between rainfall and landslide properties

We do not find a clear influence of storm metrics on landslide scar areas nor runout areas distributions. This does not necessarily imply that storm properties do not affect landslide runout or scar size, but suggest that this effect is minor compared to other factors varying between the inventories. For example, large lithological contrast exist between each events, and sometimes

25   within event (J11, TW9, Fig Suppl. 6). Variations in slope distribution and relief are also wide between each case (Fig 1, 4) and have also been reported to influence landslide size (Frattini and Crosta, 2013) since long and steep slopes amplify runout. Therefore, it is likely that only some adequate normalization of these contributions could reveal the influence of rainfall on landslide size. Given that topography and lithology change within the landslide distribution area, accurate comparison would also require to assess the spatial variations of rainfall over these zones. Last, the relative proportion of shallow and deep

30   landslides (i.e., small and large) must depend on the ratio of rain intensity over regolith hydrological properties (Iverson, 2000), allowing or impeding the occurrence of transient water accumulation pulses at shallow depth. Given that water retention and hydraulic conductivity may easily change by orders of magnitude between different environments, focusing on rainfall intensity only is likely insufficient. Thus, either conductivity should be assessed at first order or we should study various storms occurring over the same region, for example with datasets from Taiwan (Chen et al., 2013).

Finally, we observed at least two regimes of relations between landsliding and the topographical slopes, one in which landslides occur preferentially on the steepest part of the topography and the other in which the landslides occur almost uniformly on slopes beyond the topographic mode (Fig 4). It is yet unclear whether the case of Brazil 2008 with a systematic under-sampling of steep slopes is another behavior or is in the continuity of the latter type. In any case, these behaviors do not correlate with the topographic mode itself or the total landsliding. We note that in the case of earthquake triggered landslides, we systematically observe preferential landsliding on the steepest slopes (Parise and Jibson, 2000; Gorum et al., 2013, 2014)(Fig 4), quite similar to one end-member behavior. One dimensional static force balance shows that the steepest slopes are the most unstable, and therefore the over-sampling of steep slopes must be expected if the forcing (pore water pressure or shaking) is randomly distributed across the whole topography. To obtain equal sampling or under-sampling of steep slopes, the forcing intensity must be anti-correlated with slope gradient. Rainfall may be mostly independent of local slopes, but probably not the pore pressure rise that depends on the underground water circulation and thus topography. The pore pressure will thus depend crucially on vertical infiltration and drainage, but also on along-slope contributions. For example under moderate intensity, but long rainfall, pore water pressure will reach higher level in concave, downslope areas (Montgomery and Dietrich, 1994) with relatively large drainage area, and thus lower slope gradient (Montgomery, 2001). In such view, landslide slope statistics would bear information on the type of rainfall, short and intense (relative to local permeability) for steep over-sampling, while equal sampling and under-sampling would relate to moderate and long rainfall. This framework could explain the significant anti-correlation between the landslide-topography probability ratio and the storm duration (Fig 4). We tried to plot the slope-gradient vs drainage area relationship for topography and landslide subset of various events without finding clear over-sampling of high-drainage and gentle gradient ares in the landslide distribution. This may suggest another explanation has to be put forward, or simply that a 30m DEM is not able to resolve accurately the fine-scale pattern of slope and drainage on the hillsides, where landslides occur. In any case, we note that it is often suggested that short and intense rainfall should produce mostly small landslides in contrast to long, moderate rainfall (Van Asch et al., 1999), but our datasets suggest it may be easier to detect differences in the slope sampling of landslides for these storm end-members. Further constraints on the behavior of these end-members may be achieved through a discussion in terms of relative distance from ridge and river (cf, Meunier et al., 2008), as intense and brief storms should yield uniformly distributed landsliding, in contrast to longer, less intense storms favoring near river slides.

5 Conclusions

We present landslide inventories (comprising from a few hundreds to more than 15,000 events) associated with eight triggering rain storms from Asia, South America, and North America. We hypothesize that these datasets constitute a global database of rainfall-induced landslides, that allows studying a number of landslide metrics and their relations to rainfall and landscape properties. Indeed, although spanning a large range of landscape settings, whether in terms of topography, climate or vegetation, the magnitude of landsliding scales non-linearly with the magnitude of the storm, here quantified with estimates of the total rainfall. We also found that correlation between landsliding and rainfall is higher when considering landslide scar estimates

obtained through a normalization of landslide runout, as the runout distribution does not clearly correlate to rainfall. For total landsliding and maximum local landslide density, power-law scaling based on total rainfall explains 74% (87% for total volume) and 76% (95% for volume density) of the variance, respectively. Adding a number of other storm events as well as integrating other rainfall forcing parameters or landscape susceptibility properties have therefore the potential to yield robust prediction on the magnitude of rainfall induced landsliding. Last, we identify that short storm tends to trigger landslides on the steepest slopes of the landscapes while landslides induced by long storms sample equally the slope distribution, possibly relating to underground water accumulation on high drainage-low gradient portions of the hillslope. This may bring new, although less straightforward, implications for the difference in resulting topography of bedrock landscape dominated by rainfall-induced or earthquake-induced landslides (Densmore and Hovius, 2000). Although preliminary these insights and scaling clearly show the value of collecting comprehensive landslide inventories that can be related to a single storm and we identified a number of recent storm events were such type of inventory could be produced. Although not systematically addressed here, landslide density spatial pattern is likely strongly related to the spatio-temporal pattern of rainfall, and constraining the quantitative links between the two is another challenge that may be addressed with some of the inventories presented here. More generally, the database presented here may also serve as a benchmark for developing and comparing rainfall induced landslide models, whether empirical, semi- or fully-deterministic. These future developments are important challenges in order to understand the natural hazards posed by rainfall-induced landslides as well as their specific implication for the erosion and topographic evolution of landscapes in different climatic settings.

Data availability. All imagery used to map the landslides is available in public repository except the images from Formosat-2, Geoeye-1 and airphotos used for the events in Colorado, Micronesia and Japan. For the two former, landslide maps are directly available from the USGS at http://pubs.usgs.gov/of/2003/ofr-03-050/ and https://pubs.usgs.gov/of/2004/1348/. For Japan and Brazil, extensive high resolution imagery is available over most of the areas of interest in Google Earth. The new digitized landslide inventories are available upon request.

Author contributions. OM designed the study and performed all analyses with some inputs from AS, JPM and MG. TU provided landslide and rainfall data for the J11 event. SHC provided imagery and landslide data for the TW9 event. OM wrote the manuscript with contributions from all co-authors.

Competing interests. The authors declare no conflicts of interest with the present study.

References

Ardizzone, F., Basile, G., Cardinali, M., Casagli, N., Conte, S. D., Ventisette, C. D., Fiorucci, F., Garfagnoli, F., Gigli, G., Guzzetti, F., Iovine, G., Mondini, A. C., Moretti, S., Panebianco, M., Raspini, F., Reichenbach, P., Rossi, M., Tanteri, L., and Terranova, O.: Landslide inventory map for the Briga and the Giampilieri catchments, NE Sicily, Italy, Journal of Maps, 8, 176–180, https://doi.org/10.1080/17445647.2012.694271, https://doi.org/10.1080/17445647.2012.694271, 2012.

Arnone, E., Noto, L. V., Lepore, C., and Bras, R. L.: Physically-based and distributed approach to analyze rainfall-triggered landslides at watershed scale, Geomorphology, 133, 121–131, https://doi.org/10.1016/j.geomorph.2011.03.019, http://www.sciencedirect.com/science/article/pii/S0169555X11002637, 2011.

Baum, R. L., Godt, J. W., and Savage, W. Z.: Estimating the timing and location of shallow rainfall-induced landslides using a model for transient, unsaturated infiltration, Journal of Geophysical Research: Earth Surface, 115, F03 013, https://doi.org/10.1029/2009JF001321, http://onlinelibrary.wiley.com/doi/10.1029/2009JF001321/abstract, 2010.

Blodgett, T. A. and Isacks, B. L.: Landslide Erosion Rate in the Eastern Cordillera of Northern Bolivia, Earth Interactions, 11, 1–30, https://doi.org/10.1175/2007EI222.1, http://journals.ametsoc.org/doi/full/10.1175/2007EI222.1, 2007.

Bucknam, R. C., Coe, J. A., Chavarria, M. M., Godt, J. W., Tarr, A. C., Bradley, L.-A., Rafferty, S. A., Hancock, D., Dart, R. L., and Johnson, M. L.: Landslides triggered by Hurricane Mitch in Guatemala – inventory and discussion, USGS Numbered Series 2001-443, http://pubs.er.usgs.gov/publication/ofr01443, 2001.

Caine, N.: The Rainfall Intensity: Duration Control of Shallow Landslides and Debris Flows, Geografiska Annaler. Series A, Physical Geography, 62, 23–27, https://doi.org/10.2307/520449, http://www.jstor.org/stable/520449, 1980.

Camargo, L. P.: Análise integrada no meio físico dos ribeirões Braço Serafim e Máximo com ênfase nas áreas de fragilidade estrutural, Luís Alves, (SC), PhD thesis, Universidade Federal de Santa Catarina, Florianopolis, https://repositorio.ufsc.br/handle/123456789/157291, 2015.

Cannon, S. H., Haller, K. M., Ekstrom, I., Schweig, E. S., Devoli, G., Moore, D. W., Rafferty, S. A., and Tarr, A. C.: Landslide response to Hurricane Mitch rainfall in seven study areas in Nicaragua, USGS Numbered Series 2001-412-A, http://pubs.er.usgs.gov/publication/ofr01412A, 2001.

Cardinali, M., Galli, M., Guzzetti, F., Ardizzone, F., Reichenbach, P., and Bartoccini, P.: Rainfall induced landslides in December 2004 in south-western Umbria, central Italy: types, extent, damage and risk assessment, Nat. Hazards Earth Syst. Sci., 6, 237–260, https://doi.org/10.5194/nhess-6-237-2006, http://www.nat-hazards-earth-syst-sci.net/6/237/2006/, 2006.

Chang, K.-t., Chiang, S.-h., Chen, Y.-c., and Mondini, A. C.: Modeling the spatial occurrence of shallow landslides triggered by typhoons, Geomorphology, 208, 137–148, https://doi.org/10.1016/j.geomorph.2013.11.020, http://www.sciencedirect.com/science/article/pii/S0169555X13005990, 2014.

Chen, Y.-C., Chang, K.-t., Chiu, Y.-J., Lau, S.-M., and Lee, H.-Y.: Quantifying rainfall controls on catchment-scale landslide erosion in Taiwan, Earth Surface Processes and Landforms, 38, 372–382, https://doi.org/10.1002/esp.3284, http://onlinelibrary.wiley.com/doi/10.1002/esp.3284/abstract, 2013.

Chen, Y.-c., Chang, K.-t., Lee, H.-y., and Chiang, S.-h.: Average landslide erosion rate at the watershed scale in southern Taiwan estimated from magnitude and frequency of rainfall, Geomorphology, 228, 756–764, https://doi.org/10.1016/j.geomorph.2014.07.022, http://www.sciencedirect.com/science/article/pii/S0169555X14003869, 2015.

Clark, K. E., West, A. J., Hilton, R. G., Asner, G. P., Quesada, C. A., Silman, M. R., Saatchi, S. S., Farfan-Rios, W., Martin, R. E., Horwath, A. B., Halladay, K., New, M., and Malhi, Y.: Storm-triggered landslides in the Peruvian Andes and implications for topography, carbon cycles, and biodiversity, Earth Surface Dynamics, 4, 47–70, https://doi.org/10.5194/esurf-4-47-2016, http://www.earth-surf-dynam.net/4/47/2016/, 2016.

5   Crone, A. J., Baum, R. L., Lidke, D. J., Sather, D. N., Bradley, L.-A., and Tarr, A. C.: Landslides induced by Hurricane Mitch in El Salvador – an inventory and descriptions of selected features, USGS Numbered Series 2001-444, http://pubs.er.usgs.gov/publication/ofr01444, 2001.

Dahal, R. K. and Hasegawa, S.: Representative rainfall thresholds for landslides in the Nepal Himalaya, Geomorphology, 100, 429–443, https://doi.org/10.1016/j.geomorph.2008.01.014, http://www.sciencedirect.com/science/article/pii/S0169555X08000172, 2008.

Densmore, A. L. and Hovius, N.: Topographic fingerprints of bedrock landslides, Geology, 28, 371–374, https://doi.org/10.1130/0091-
10   7613(2000)28<371:TFOBL>;2.0.CO;2, http://geology.geoscienceworld.org/content/28/4/371, 2000.

Frattini, P. and Crosta, G. B.: The role of material properties and landscape morphology on landslide size distributions, Earth and Planetary Science Letters, 361, 310–319, https://doi.org/10.1016/j.epsl.2012.10.029, http://www.sciencedirect.com/science/article/pii/S0012821X12005985, 2013.

Gabet, E. J., Burbank, D. W., Putkonen, J. K., Pratt-Sitaula, B. A., and Ojha, T.: Rainfall thresholds for landsliding in the Himalayas of
15   Nepal, Geomorphology, 63, 131–143, https://doi.org/10.1016/j.geomorph.2004.03.011, http://www.sciencedirect.com/science/article/pii/S0169555X04001114, 2004.

Gariano, S. L. and Guzzetti, F.: Landslides in a changing climate, Earth-Science Reviews, 162, 227–252, https://doi.org/10.1016/j.earscirev.2016.08.011, http://www.sciencedirect.com/science/article/pii/S0012825216302458, 2016.

Godt, J. W. and Coe, J. A.: Alpine debris flows triggered by a 28 July 1999 thunderstorm in the central Front Range, Colorado, Geomorphol-
20   ogy, 84, 80–97, https://doi.org/10.1016/j.geomorph.2006.07.009, http://www.sciencedirect.com/science/article/pii/S0169555X06002868, 2007.

Godt, J. W., Baum, R. L., and Chleborad, A. F.: Rainfall characteristics for shallow landsliding in Seattle, Washington, USA, Earth Surface Processes and Landforms, 31, 97–110, https://doi.org/10.1002/esp.1237, http://onlinelibrary.wiley.com/doi/10.1002/esp.1237/abstract, 2006.

25   Gorum, T., van Westen, C. J., Korup, O., van der Meijde, M., Fan, X., and van der Meer, F. D.: Complex rupture mechanism and topography control symmetry of mass-wasting pattern, 2010 Haiti earthquake, Geomorphology, 184, 127–138, https://doi.org/10.1016/j.geomorph.2012.11.027, http://www.sciencedirect.com/science/article/pii/S0169555X12005478, 2013.

Gorum, T., Korup, O., van Westen, C. J., van der Meijde, M., Xu, C., and van der Meer, F. D.: Why so few? Landslides triggered by the 2002 Denali earthquake, Alaska, Quaternary Science Reviews, 95, 80–94, https://doi.org/10.1016/j.quascirev.2014.04.032, http://www.
30   sciencedirect.com/science/article/pii/S0277379114001632, 2014.

Guzzetti, F., Cardinali, M., Reichenbach, P., Cipolla, F., Sebastiani, C., Galli, M., and Salvati, P.: Landslides triggered by the 23 November 2000 rainfall event in the Imperia Province, Western Liguria, Italy, Engineering Geology, 73, 229–245, https://doi.org/10.1016/j.enggeo.2004.01.006, http://www.sciencedirect.com/science/article/pii/S0013795204000225, 2004.

Guzzetti, F., Peruccacci, S., Rossi, M., and Stark, C. P.: The rainfall intensity–duration control of shallow landslides and debris flows:
35   an update, Landslides, 5, 3–17, https://doi.org/10.1007/s10346-007-0112-1, http://link.springer.com/article/10.1007/s10346-007-0112-1, 2008.

Harp, E. L., Hagaman, K. W., Held, M. D., and McKenna, J. P.: Digital inventory of landslides and related deposits in Honduras triggered by Hurricane Mitch, USGS Numbered Series 2002-61, U.S. Geological Survey, Reston, VA, http://pubs.er.usgs.gov/publication/ofr0261, 2002.

Harp, E. L., Reid, M. E., and Michael, J. A.: Hazard analysis of landslides triggered by Typhoon Chata'an on July 2, 2002, in Chuuk State, Federated States of Micronesia, USGS Numbered Series 2004-1348, http://pubs.er.usgs.gov/publication/ofr20041348, 2004.

Hovius, N., Stark, C. P., and Allen, P. A.: Sediment flux from a mountain belt derived by landslide mapping, Geology, 25, 231–234, https://doi.org/10.1130/0091-7613(1997)025<0231:SFFAMB>2.3.CO;2, http://geology.geoscienceworld.org/content/25/3/231, 1997.

Huffman, G. J., Bolvin, D. T., Nelkin, E. J., Wolff, D. B., Adler, R. F., Gu, G., Hong, Y., Bowman, K. P., and Stocker, E. F.: The TRMM Multisatellite Precipitation Analysis (TMPA): Quasi-Global, Multiyear, Combined-Sensor Precipitation Estimates at Fine Scales, Journal of Hydrometeorology, 8, 38–55, https://doi.org/10.1175/JHM560.1, https://journals.ametsoc.org/doi/abs/10.1175/JHM560.1, 2007.

Iverson, R. M.: Landslide triggering by rain infiltration, Water Resources Research, 36, 1897–1910, https://doi.org/10.1029/2000WR900090, http://onlinelibrary.wiley.com/doi/10.1029/2000WR900090/abstract, 2000.

Jibson, R. W., Prentice, C. S., Borissoff, B. A., Rogozhin, E. A., and Langer, C. J.: Some observations of landslides triggered by the 29 April 1991 Racha earthquake, Republic of Georgia, Bulletin of the Seismological Society of America, 84, 963–973, http://bssa.geoscienceworld.org/content/84/4/963, 1994.

Jibson, R. W., Harp, E. L., and Michael, J. A.: A method for producing digital probabilistic seismic landslide hazard maps, Engineering Geology, 58, 271–289, https://doi.org/10.1016/S0013-7952(00)00039-9, http://www.sciencedirect.com/science/article/pii/S0013795200000399, 2000.

Katz, O., Morgan, J. K., Aharonov, E., and Dugan, B.: Controls on the size and geometry of landslides: Insights from discrete element numerical simulations, Geomorphology, 220, 104–113, https://doi.org/10.1016/j.geomorph.2014.05.021, http://www.sciencedirect.com/science/article/pii/S0169555X1400289X, 2014.

Keefer, D. K., Wilson, R. C., Mark, R. K., Brabb, E. E., Brown, W. M., Ellen, S. D., Harp, E. L., Wieczorek, G. F., Alger, C. S., and Zatkin, R. S.: Real-Time Landslide Warning During Heavy Rainfall, Science, 238, 921–925, https://doi.org/10.1126/science.238.4829.921, http://science.sciencemag.org/content/238/4829/921, 1987.

Kirschbaum, D., Adler, R., Adler, D., Peters-Lidard, C., and Huffman, G.: Global Distribution of Extreme Precipitation and High-Impact Landslides in 2010 Relative to Previous Years, Journal of Hydrometeorology, 13, 1536–1551, https://doi.org/10.1175/JHM-D-12-02.1, http://journals.ametsoc.org/doi/abs/10.1175/JHM-D-12-02.1, 2012.

Kirschbaum, D. B., Adler, R., Hong, Y., Hill, S., and Lerner-Lam, A.: A global landslide catalog for hazard applications: method, results, and limitations, Natural Hazards, 52, 561–575, https://doi.org/10.1007/s11069-009-9401-4, http://link.springer.com/article/10.1007/s11069-009-9401-4, 2009.

Kubota, T., Shige, S., Hashizume, H., Ushio, T., Aonashi, K., Kachi, M., and Okamoto, K.: Global Precipitation Map using Satelliteborne Microwave Radiometers by the GSMaP Project : Production and Validation, in: 2006 IEEE MicroRad, pp. 290–295, https://doi.org/10.1109/MICRAD.2006.1677106, 2006.

Lafore, J. P., Stein, J., Asencio, N., Bougeault, P., Ducrocq, V., Duron, J., Fischer, C., Héreil, P., Mascart, P., Masson, V., Pinty, J. P., Redelsperger, J. L., Richard, E., and Arellano, J. V.-G. d.: The Meso-NH Atmospheric Simulation System. Part I: adiabatic formulation and control simulations, Annales Geophysicae, 16, 90–109, https://doi.org/10.1007/s00585-997-0090-6, https://link.springer.com/article/10.1007/s00585-997-0090-6, 1997.

Larsen, I., Montgomery, D., and Korup, O.: Landslide erosion controlled by hillslope material, Nature Geoscience, 3, 247–251, 2010.

Lehmann, P. and Or, D.: Hydromechanical triggering of landslides: From progressive local failures to mass release, Water Resources Research, 48, W03 535, https://doi.org/10.1029/2011WR010947, http://onlinelibrary.wiley.com/doi/10.1029/2011WR010947/abstract, 2012.

Liao, H.-W. and Lee, C.: Landslides triggered by Chi-Chi earthquake, in: Proceedings of the 21st Asian conference on remote sensing, vol. 1, pp. 383–388, 2000.

Malamud, B. D., Turcotte, D. L., Guzzetti, F., and Reichenbach, P.: Landslide inventories and their statistical properties, Earth Surface Processes and Landforms, 29, 687–711, https://doi.org/10.1002/esp.1064, http://onlinelibrary.wiley.com/doi/10.1002/esp.1064/abstract, 2004.

Marc, O. and Hovius, N.: Amalgamation in landslide maps: effects and automatic detection, Nat. Hazards Earth Syst. Sci., 15, 723–733, https://doi.org/10.5194/nhess-15-723-2015, http://www.nat-hazards-earth-syst-sci.net/15/723/2015/, 2015.

Marc, O., Hovius, N., Meunier, P., Uchida, T., and Hayashi, S.: Transient changes of landslide rates after earthquakes, Geology, 43, 883–886, https://doi.org/10.1130/G36961.1, http://geology.geoscienceworld.org/content/early/2015/08/21/G36961.1, 2015.

Marc, O., Hovius, N., Meunier, P., Gorum, T., and Uchida, T.: A seismologically consistent expression for the total area and volume of earthquake-triggered landsliding, Journal of Geophysical Research: Earth Surface, 121, 640–663, https://doi.org/10.1002/2015JF003732, http://onlinelibrary.wiley.com/doi/10.1002/2015JF003732/abstract, 2016.

Marc, O., Meunier, P., and Hovius, N.: Prediction of the area affected by earthquake-induced landsliding based on seismological parameters, Nat. Hazards Earth Syst. Sci., 17, 1159–1175, https://doi.org/10.5194/nhess-17-1159-2017, https://www.nat-hazards-earth-syst-sci.net/17/1159/2017/, 2017.

Meunier, P., Hovius, N., and Haines, A. J.: Regional patterns of earthquake-triggered landslides and their relation to ground motion, Geophysical Research Letters, 34, L20 408, https://doi.org/10.1029/2007GL031337, http://onlinelibrary.wiley.com/doi/10.1029/2007GL031337/abstract, 2007.

Meunier, P., Hovius, N., and Haines, J. A.: Topographic site effects and the location of earthquake induced landslides, Earth and Planetary Science Letters, 275, 221–232, https://doi.org/10.1016/j.epsl.2008.07.020, http://www.sciencedirect.com/science/article/pii/S0012821X08004536, 2008.

Meunier, P., Uchida, T., and Hovius, N.: Landslide patterns reveal the sources of large earthquakes, Earth and Planetary Science Letters, 363, 27–33, https://doi.org/10.1016/j.epsl.2012.12.018, http://www.sciencedirect.com/science/article/pii/S0012821X12007042, 2013.

Milledge, D. G., Bellugi, D., McKean, J. A., Densmore, A. L., and Dietrich, W. E.: A multidimensional stability model for predicting shallow landslide size and shape across landscapes, Journal of Geophysical Research: Earth Surface, 119, 2014JF003 135, https://doi.org/10.1002/2014JF003135, http://onlinelibrary.wiley.com/doi/10.1002/2014JF003135/abstract, 2014.

Mondini, A. C.: Measures of Spatial Autocorrelation Changes in Multitemporal SAR Images for Event Landslides Detection, Remote Sensing, 9, 554, https://doi.org/10.3390/rs9060554, http://www.mdpi.com/2072-4292/9/6/554, 2017.

Montgomery, D. R.: Slope Distributions, Threshold Hillslopes, and Steady-state Topography, American Journal of Science, 301, 432–454, https://doi.org/10.2475/ajs.301.4-5.432, http://www.ajsonline.org/content/301/4-5/432, 2001.

Montgomery, D. R. and Dietrich, W. E.: A physically based model for the topographic control on shallow landsliding, Water Resources Research, 30, 1153–1171, https://doi.org/10.1029/93WR02979, http://onlinelibrary.wiley.com/doi/10.1029/93WR02979/abstract, 1994.

Netto, A. L. C., Sato, A. M., Avelar, A. d. S., Vianna, L. G. G., Araújo, I. S., Ferreira, D. L. C., Lima, P. H., Silva, A. P. A., and Silva, R. P.: January 2011: The Extreme Landslide Disaster in Brazil, in: Landslide Science and Practice, pp. 377–384, Springer, Berlin, Heidelberg, https://link.springer.com/chapter/10.1007/978-3-642-31319-6_51, dOI: 10.1007/978-3-642-31319-6_51, 2013.

Nowicki, M. A., Wald, D. J., Hamburger, M. W., Hearne, M., and Thompson, E. M.: Development of a globally applicable model for near real-time prediction of seismically induced landslides, Engineering Geology, 173, 54–65, https://doi.org/10.1016/j.enggeo.201s4.02.002, http://www.sciencedirect.com/science/article/pii/S0013795214000301, 2014.

Ono, K., Kazama, S., and Ekkawatpanit, C.: Assessment of rainfall-induced shallow landslides in Phetchabun and Krabi provinces, Thailand, Natural Hazards, 74, 2089–2107, https://doi.org/10.1007/s11069-014-1292-3, https://link.springer.com/article/10.1007/s11069-014-1292-3, 2014.

Parise, M. and Jibson, R. W.: A seismic landslide susceptibility rating of geologic units based on analysis of characteristics of landslides triggered by the 17 January, 1994 Northridge, California earthquake, Engineering Geology, 58, 251–270, https://doi.org/10.1016/S0013-7952(00)00038-7, http://www.sciencedirect.com/science/article/pii/S0013795200000387, 2000.

Petley, D.: Global patterns of loss of life from landslides, Geology, 40, 927–930, https://doi.org/10.1130/G33217.1, http://geology.geoscienceworld.org/content/40/10/927, 2012.

Pozzobon, M.: ANÁLISE DA SUSCETIBILIDADE A DESLIZAMENTOS NO MUNICÍPIO DE BLUMENAU/SC: UMA ABORDAGEM PROBABILÍSTICA ATRAVÉS DA APLICAÇÃO DA TÉCNICA PESOS DE EVIDÊNCIA., PhD thesis, UNIVERSIDADE FEDERAL DO PARANÁ, Curitiba, http://www.floresta.ufpr.br/defesas/pdf_dr/2013/t342_0370-D.pdf, 2013.

Reid, L. M.: Calculation of average landslide frequency using climatic records, Water Resources Research, 34, 869–877, https://doi.org/10.1029/97WR02682, http://onlinelibrary.wiley.com/doi/10.1029/97WR02682/abstract, 1998.

Reid, L. M. and Page, M. J.: Magnitude and frequency of landsliding in a large New Zealand catchment, Geomorphology, 49, 71–88, https://doi.org/10.1016/S0169-555X(02)00164-2, http://www.sciencedirect.com/science/article/pii/S0169555X02001642, 2003.

Saito, H. and Matsuyama, H.: Catastrophic Landslide Disasters Triggered by Record-Breaking Rainfall in Japan: Their Accurate Detection with Normalized Soil Water Index in the Kii Peninsula for the Year 2011, Sola, 8, 81–84, https://doi.org/10.2151/sola.2012-021, 2012.

Saito, H., Korup, O., Uchida, T., Hayashi, S., and Oguchi, T.: Rainfall conditions, typhoon frequency, and contemporary landslide erosion in Japan, Geology, 42, 999–1002, https://doi.org/10.1130/G35680.1, http://geology.geoscienceworld.org/content/42/11/999, 2014.

Schmidt, K. M. and Montgomery, D. R.: Limits to Relief, Science, 270, 617–620, https://doi.org/10.1126/science.270.5236.617, http://www.sciencemag.org/content/270/5236/617, 1995.

Stark, C. P. and Guzzetti, F.: Landslide rupture and the probability distribution of mobilized debris volumes, Journal of Geophysical Research: Earth Surface, 114, F00A02, https://doi.org/10.1029/2008JF001008, http://onlinelibrary.wiley.com/doi/10.1029/2008JF001008/abstract, 2009.

Stark, C. P. and Hovius, N.: The characterization of landslide size distributions, Geophysical Research Letters, 28, 1091–1094, https://doi.org/10.1029/2000GL008527, http://onlinelibrary.wiley.com/doi/10.1029/2000GL008527/abstract, 2001.

Stumpf, A., Lachiche, N., Malet, J.-P., Kerle, N., and Puissant, A.: Active Learning in the Spatial Domain for Remote Sensing Image Classification, IEEE Transactions on Geoscience and Remote Sensing, 52, 2492–2507, https://doi.org/10.1109/TGRS.2013.2262052, 2014.

Tanyaş, H., van Westen, C. J., Allstadt, K. E., Anna Nowicki Jessee, M., Görüm, T., Jibson, R. W., Godt, J. W., Sato, H. P., Schmitt, R. G., Marc, O., and Hovius, N.: Presentation and Analysis of a Worldwide Database of Earthquake-Induced Landslide Inventories, Journal of Geophysical Research: Earth Surface, 122, 2017JF004 236, https://doi.org/10.1002/2017JF004236, http://onlinelibrary.wiley.com/doi/10.1002/2017JF004236/abstract, 2017.

Uchida, T., Tamur, K., and Akiyama, K.: THE ROLE OF GRID CELL SIZE, FLOW ROUTING ALGOLITHM AND SPATIAL VARI-ABILITY OF SOIL DEPTH ON SHALLOW LANDSLIDE PREDICTION, in: 5th International Conference on Debris-Flow Hazards

Mitigation: Mechanics, Prediction and Assessment, pp. 149–157, ITALIAN JOURNAL OF ENGINEERING GEOLOGY AND ENVI-RONMENT, Padua, Italy, 2011.

Uchida, T., Sato, T., Mizuno, M., and Okamoto, A.: The role of rainfall magnitude on landslide characteristics triggered by Typhoon Tales, 2011 Civil engineering journal : 54(10), 10-13, 2012, Civil Engineering Journal (in Japanese), 54, 10–13, 2012.

5 Uchida, T., Okamoto, A., Kanbara, J. I., and Kuramoto, K.: RAINFALL THRESHOLDS FOR DEEP-SEATED RAPID LANDSLIDES, in: International Conference on Vajont 1963-2013 / Proceedings - Thoughts and analyses after 50 years since the catastrophic landslide, pp. 211–217, ITALIAN JOURNAL OF ENGINEERING GEOLOGY AND ENVIRONMENT, Padua, Italy, 2013.

Ushio, T., Sasashige, K., Kubota, T., Shige, S., Okamoto, K., Aonashi, K., Inoue, T., Takahashi, N., Iguchi, T., Kachi, M., Oki, R., Morimoto, T., and Kawasaki, Z.-I.: A Kalman Filter Approach to the Global Satellite Mapping of Precipitation (GSMaP) from Com-

10 bined Passive Microwave and Infrared Radiometric Data, Journal of the Meteorological Society of Japan. Ser. II, 87A, 137–151, https://doi.org/10.2151/jmsj.87A.137, https://www.jstage.jst.go.jp/article/jmsj/87A/0/87A_0_137/_article, 2009.

Van Asch, T. W. J., Buma, J., and Van Beek, L. P. H.: A view on some hydrological triggering systems in landslides, Geomorphology, 30, 25–32, https://doi.org/10.1016/S0169-555X(99)00042-2, http://www.sciencedirect.com/science/article/pii/S0169555X99000422, 1999.

Wilson, R. C. and Wieczorek, G. F.: Rainfall Thresholds for the Initiation of Debris Flows at La Honda, California, Environmental &

15 Engineering Geoscience, I, 11–27, https://doi.org/10.2113/gseegeosci.I.1.11, http://eeg.geoscienceworld.org/content/I/1/11, 1995.

Yagi, H., Sato, G., Higaki, D., Yamamoto, M., and Yamasaki, T.: Distribution and characteristics of landslides induced by the Iwate–Miyagi Nairiku Earthquake in 2008 in Tohoku District, Northeast Japan, Landslides, 6, 335–344, 2009.